The Journal of Chemical Physics

RESEARCH ARTICLE | FEBRUARY 11 2026

Finite elements and moving asymptotes accelerate quantum optimal control—FEMMA

Mengjia He ; Yongbo Deng ; Burkhard Luy ; Jan G. Korvink

J. Chem. Phys. 164, 064114 (2026)
https://doi.org/10.1063/5.0305310

AIP Publishing

The Journal of Chemical Physics

ARTICLE

pubs.aip.org/aip/jcp

Finite elements and moving asymptotes accelerate quantum optimal control—FEMMA

Cite as: J. Chem. Phys. 164, 064114 (2026); doi: 10.1063/5.0305310
Submitted: 5 October 2025 • Accepted: 20 January 2026 •
Published Online: 11 February 2026

View Online Export Citation CrossMark

Mengjia He,[1] Yongbo Deng,[1] Burkhard Luy,[2,3] and Jan G. Korvink[1,a)]

AFFILIATIONS

[1] Institute of Microstructure Technology, Karlsruhe Institute of Technology, Eggenstein-Leopoldshafen, Germany
[2] Institute for Biological Interfaces 4—Magnetic Resonance, Karlsruhe Institute of Technology, Eggenstein-Leopoldshafen, Germany
[3] Institute of Organic Chemistry, Karlsruhe Institute of Technology, Karlsruhe, Germany

[a)] Author to whom correspondence should be addressed: jan.korvink@kit.edu

ABSTRACT

Quantum optimal control is central to designing spin manipulation pulses. Gradient-based pulse optimization can be facilitated by either accelerating gradient evaluation or enhancing the convergence rate. In this work, we accelerated single-spin optimal control by combining the finite element method with the method of moving asymptotes. By treating discretized time as spatial coordinates, the Liouville–von Neumann equation was reformulated as a linear system, efficiently yielding a joint solution of the spin trajectory and control gradient. The method of moving asymptotes, relying on the ensemble fidelities and gradients, achieves rapid convergence for a target fidelity of 0.995.

I. INTRODUCTION

In magnetic resonance spectroscopy (MRS) and imaging (MRI), shaped radio frequency (RF) pulses are widely employed to drive the state of a spin system toward a desired target. The design of such pulses is typically framed as an optimal control problem.[1]

Among gradient-based optimization techniques, the gradient ascent pulse engineering (GRAPE) method[2] has become one of the most widely used and efficient methods. The original GRAPE method discretizes the control time into piecewise-constant intervals and computes the spin trajectory via a bi-directional propagation, where gradients are obtained using a first-order finite-difference approximation under sufficiently fine time slicing.

A variety of extensions to GRAPE have since been developed, targeting more accurate derivative computation, advanced optimization strategies, and broader applicability to general quantum systems. The derivatives of the sub-propagator to control variables have been derived by differentiating the Taylor series.[3] A higher-order finite difference method was introduced to improve gradient accuracy.[4] The auxiliary matrix formalism (AUXMAT) was introduced to compute exact gradients and Hessians, leading to improved convergence.[5] Automatic differentiation, implemented on graphics processing units, was introduced to accelerate gradient computation.[6,7] Beyond the gradient-descent update of the original formulation, several optimization algorithms have been incorporated into GRAPE frameworks, including Quasi-Newton approaches,[4,8,9] such as the Broyden–Fletcher–Goldfarb–Shanno (BFGS) algorithm and its limited-memory version (L-BFGS), and Newton–Raphson methods[10] that provide quadratic convergence. The accelerated Newton–Raphson variant was developed to reduce the Hessian evaluation to $O(N)$ complexity, as demonstrated for a single-spin system.[11] Extension algorithms for open quantum systems demonstrated high-fidelity control when handling decoherence effects.[7,12]

As modern magnetic resonance systems operate at increasingly higher frequencies, various instrumental limitations have become more prominent, including RF power constraints[13–15] and hardware-induced distortions.[16–19] Optimization problems also grow more complex when modeling multi-qubit systems exhibiting entanglement,[20] heteronuclear spin systems with J-coupling,[21] or crystalline orientation distributions in solid-state MRS.[22] In parallel transmit MRI, pulse design under safety constraints can involve thousands of control variables and hundreds of spatial voxels.[23–25] To address crosstalk in parallel MRS, compensation strategies incorporate an ensemble of B_0 distortions caused by gradient coils,[26] along with multiple cooperative pulses tailored for parallel excitation.[27]

These scenarios often require ensemble-based optimization, where system parameters vary across ensemble members. In such cases, the gradient or Hessian must be computed for each ensemble element and control updates are determined from the ensemble-averaged derivatives, as in the L-BFGS and Newton methods. This significantly increases the computational cost, potentially requiring several hours or even days of high-performance computing time.

In this work, we address the optimization of single-spin magnetic resonance pulses by combining the finite element method (FEM)[28,29] with the method of moving asymptotes (MMA).[30] Finite elements with linear, quadratic, and cubic Hermite basis functions provide an efficient and scalable solution for computing single-spin optimal-control gradients. By formulating the ensemble-averaged fidelity maximization as a constrained optimization, MMA converges more rapidly than L-BFGS and yields the lowest overall runtime among L-BFGS and Newton–Raphson methods.

II. METHODOLOGY

The Liouville–von Neumann (LvN) equation masters the evolution of a general spin system. The equation in Liouville space is given by

$$\begin{aligned} \frac{d}{dt}\boldsymbol{\rho}(t) + \mathrm{i}\mathbf{L}\boldsymbol{\rho}(t) &= 0, \\ \boldsymbol{\rho}(0) &= \boldsymbol{\rho}_0, \end{aligned} \tag{1}$$

where $\boldsymbol{\rho}_0$ is the initial state. While ignoring the relaxation effect, the Liouvillian $\mathbf{L}$ can be decomposed into the internal part and the control part,

$$\mathbf{L}(t) = \mathbf{L}_{\mathrm{int}}(t) + \sum_m x_m(t)\mathbf{L}_m, \tag{2}$$

where $\mathbf{L}_{\mathrm{int}}$ could contain Zeeman interaction with the magnetic field and spin–spin couplings. $\mathbf{L}_m$ represents a control operator, and $x_m(t)$ is a time-dependent coefficient. A control sequence $\boldsymbol{x}(t)$ is applied to steer the spin system from an initial state $\boldsymbol{\rho_0}$ to a target state $\boldsymbol{\sigma}$ in a specified time duration T. A measurement of the control efficiency is the overlap between the target state and the actual final state $\boldsymbol{\rho_T}$, i.e.,

$$\eta = \langle \boldsymbol{\sigma} | \boldsymbol{\rho_T} \rangle, \tag{3}$$

which satisifies $-1 \le \eta \le 1$. We consider an ensemble spin system with N_{ens} members, for which the control amplitudes are limited, so that the optimal control problem can be defined as

$$\begin{cases} \text{Find}\, \boldsymbol{x}(t),\ t \in [0, T], \\ \text{to maximize } f = \displaystyle\sum_{k=1}^{N_{\mathrm{ens}}} \eta_k, \\ \text{constrained by } |x_m(t)| \le x_m^{\max}. \end{cases} \tag{4}$$

A. FEM solution of the Liouville–von Neumann equation

In the context of magnetic resonance, the FEM has previously been applied to solve the stochastic Liouville equation for chemically induced spin polarization problems[31,32] and for electron spin resonance spectral simulations.[33] In Eq. (1), the spatial variables are absent relative to the stochastic Liouville equation. Within the Hamilton principle, the integration domain, time interval $[0, T]$, is discretized into N elements with $N + 1$ nodes. The control variables are represented as a piecewise-constant waveform $\mathbf{x}$, rendering the Liouvillian $\mathbf{L}$ constant within each element. The solution of Eq. (1) is approximated as a linear combination of shape functions,

$$\boldsymbol{\rho}(t) = \sum_{j=1}^{N+1} \boldsymbol{\alpha}_j \phi_j(t), \tag{5}$$

where $\boldsymbol{\alpha}_j$ has the same dimension as the spin state vector $\boldsymbol{\rho}(t)$ and $\phi_j(t)$ represents the jth shape function. As shown in Fig. 1, by using the linear elements, the nodal shape functions globally defined at node j are expressed as

$$\phi_j^n(t) = \begin{cases} (t - t_{j-1})/\Delta t, & t_{j-1} \le t \le t_j, \\ (t_{j+1} - t)/\Delta t, & t_j \le t \le t_{j+1}, \\ 0, & \text{otherwise.} \end{cases} \tag{6}$$

Note that it is also possible to define the two linear shape functions locally at element j as

$$\phi_j^{e1}(t) = (t - t_j)/\Delta t, \quad \phi_j^{e2}(t) = (t_j + \Delta t - t)/\Delta t, \quad t_j \le t \le t_j + \Delta t. \tag{7}$$

In the following derivation, globally defined shape functions are used and the subscript n is omitted.

Galerkin's method[34] demonstrated that the integral of the weighted residual equals zero, i.e.,

$$\int_0^T \left(\frac{d\boldsymbol{\rho}}{dt} + \mathrm{i}\mathbf{L}\boldsymbol{\rho} \right) \hat{\omega}\, dt = 0, \tag{8}$$

where $\boldsymbol{\rho}$ is the approximated solution expressed by Eq. (5) and $\hat{\omega}$ is the chosen weighting function. Selecting each shape function as the weighting function, i.e., $\hat{\omega} = \phi_j$, and substituting Eq. (5) into Eq. (8) gives the following linear equations:

$$\sum_{j=1}^{N+1} \boldsymbol{\alpha}_j \int_0^T \left(\frac{d\phi_j}{dt} + \mathrm{i}\mathbf{L}\phi_j \right) \phi_i\, dt = 0, \quad i = 1, \ldots, N + 1. \tag{9}$$

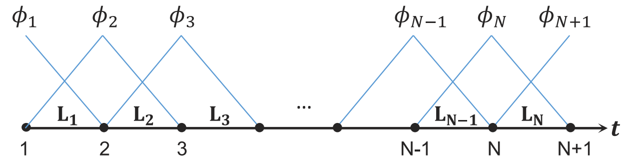

FIG. 1. View of the one-dimensional linear Lagrange global shape functions. The time interval between two nodes is uniformly set to Δt. The labels $\mathbf{L}_1, \mathbf{L}_2, \ldots, \mathbf{L}_N$ represent the discretized Liouvillian for a piecewise-constant waveform.

In matrix form, this can be written compactly as

$$\mathbf{K} \cdot \boldsymbol{\alpha} = \mathbf{f}, \tag{10}$$

where $\boldsymbol{\alpha}$ is the vectorized $\boldsymbol{\alpha}_j$ $(j = 1, 2, \ldots, N+1)$, $\mathbf{f} = 0$ is a forcing function, often called the load vector, and $\mathbf{K}$ is an impedance function, often called the stiffness matrix. The terms load and stiffness appeared first in the finite element literature because of the application to computational mechanics. An element of $\mathbf{K}$ is given by

$$K_{ij} = \int_0^T \left(\frac{d\phi_j}{dt} + \mathrm{i}\mathbf{L}\phi_j\right)\phi_i \, dt = \sum_{n=1}^{N} \int_{t_n}^{t_{n+1}} \left(\frac{d\phi_j}{dt} + \mathrm{i}\mathbf{L}\phi_j\right)\phi_i \, dt. \tag{11}$$

Considering that ϕ_j is nonzero only within the elements connected to node j, the global stiffness matrix $\mathbf{K}$ can be assembled from the element stiffness matrices,

$$\mathbf{K} = \begin{bmatrix} K_{11}^{e,1} & K_{12}^{e,1} & & & & & \\ K_{21}^{e,1} & K_{22}^{e,1} + K_{11}^{e,2} & K_{12}^{e,2} & & & & \\ & K_{21}^{e,2} & K_{22}^{e,2} + K_{11}^{e,3} & K_{12}^{e,3} & & & \\ & & K_{21}^{e,3} & \ddots & & & \\ & & & & K_{22}^{e,N-1} + K_{11}^{e,N} & K_{12}^{e,N} \\ & & & & K_{21}^{e,N} & K_{22}^{e,N} \end{bmatrix}, \tag{12}$$

which reveals its banded structure, while the stiffness matrix of the jth element is given by

$$K^{e,j} = \begin{bmatrix} \int_{t_j}^{t_{j+1}} \left(\frac{d\phi_j}{dt} + \mathrm{i}\mathbf{L}\phi_j\right)\phi_j \, dt & \int_{t_j}^{t_{j+1}} \left(\frac{d\phi_{j+1}}{dt} + \mathrm{i}\mathbf{L}\phi_{j+1}\right)\phi_j \, dt \\ \int_{t_j}^{t_{j+1}} \left(\frac{d\phi_j}{dt} + \mathrm{i}\mathbf{L}\phi_j\right)\phi_{j+1} \, dt & \int_{t_j}^{t_{j+1}} \left(\frac{d\phi_{j+1}}{dt} + \mathrm{i}\mathbf{L}\phi_{j+1}\right)\phi_{j+1} \, dt \end{bmatrix}. \tag{13}$$

Substituting the expressions for the linear shape functions yields

$$K^{e,j} = \begin{bmatrix} -\frac{\mathbf{E}}{2} + \frac{\mathrm{i}\mathbf{L}}{3}\Delta t & \frac{\mathbf{E}}{2} + \frac{\mathrm{i}\mathbf{L}}{6}\Delta t \\ -\frac{\mathbf{E}}{2} + \frac{\mathrm{i}\mathbf{L}}{6}\Delta t & \frac{\mathbf{E}}{2} + \frac{\mathrm{i}\mathbf{L}}{3}\Delta t \end{bmatrix}. \tag{14}$$

Equation (14) defines the element stiffness matrix derived from a general Liouvillian. For a single-spin system, the nodal spin vector is $\boldsymbol{\rho} \in \mathbb{C}^{4\times 1}$, the nodal Liouvillian is $\mathbf{L} \in \mathbb{C}^{4\times 4}$, and $\mathbf{E}$ denotes the identity matrix. Each element stiffness matrix $K^{e,j} \in \mathbb{C}^{8\times 8}$ couples two nodes, while the corresponding global stiffness matrix is $\mathbf{K} \in \mathbb{C}^{(4N+4)\times(4N+4)}$. The spin trajectory is obtained through four steps, as presented in Algorithm 1.

ALGORITHM 1. Solve the linear system.

```
**Input:** Initial state $\boldsymbol{\rho}_0$, stiffness matrix $\mathbf{K}$, and load vector $\mathbf{f}$
**Output:** Solution vector $\boldsymbol{\alpha}$
Initialize $\boldsymbol{\alpha}_{1:4} \leftarrow \boldsymbol{\rho}_0$;
Update load vector: $\mathbf{f} \leftarrow \mathbf{f} - \mathbf{K}_{[:,1:4]}\boldsymbol{\rho}_0$;
Modify stiffness matrix: $\mathbf{K} \leftarrow \begin{bmatrix} \mathbb{E}_4 & \\ & \mathbf{K}_{[5:4N+4,\ 5:4N+4]} \end{bmatrix}$;
Solve linear system: $\mathbf{K}\boldsymbol{\alpha} = \mathbf{f}$
```

The above-mentioned formulation is based on linear shape functions, but higher-order elements can be used to improve accuracy. For example, quadratic elements provide a finer discretization of the time axis but double the size of the stiffness matrix compared with linear elements. When a piecewise-linear waveform is employed to mitigate instrumental distortions,[17] the Hamiltonian must remain continuous across time intervals. Hermite shape functions enforce C^1 continuity between elements and are, therefore, well suited to this purpose. The stiffness matrices corresponding to quadratic elements and Hermite elements are given in Secs. S1 and S2 of the supplementary material, respectively.

B. Adjoint analysis

For compatibility with the FEM solution, the fidelity function in Eq. (3) is rewritten as

$$\eta = \sigma^\dagger \cdot \rho_T = \begin{bmatrix} \mathbf{0} & \sigma^\dagger \end{bmatrix} \cdot \boldsymbol{\alpha}, \tag{15}$$

where $\boldsymbol{\rho}_T = \boldsymbol{\alpha}_{4N+1:4N+4}$ denotes the final state. The gradient of the objective with respect to the control variables $\mathbf{x}$ is

$$\frac{d\eta}{d\mathbf{x}} = \frac{d\eta}{d\boldsymbol{\alpha}}\frac{d\boldsymbol{\alpha}}{d\mathbf{x}} = \frac{d\eta}{d\boldsymbol{\alpha}}\mathbf{K}^{-1}\left(\frac{d\mathbf{f}}{d\mathbf{x}} - \frac{d\mathbf{K}}{d\mathbf{x}}\boldsymbol{\alpha}\right). \tag{16}$$

On the right-hand side, evaluating the third term $d\mathbf{f}/d\mathbf{x} - (d\mathbf{K}/d\mathbf{x})\boldsymbol{\alpha}$ requires N matrix–vector multiplications. Since the finite elements are aligned with the discrete waveform, over which the Hamiltonian is constant, this term can be computed locally on each element, using the trajectory associated with the corresponding nodes. For instance, when $j = 1$,

$$\frac{\partial \mathbf{f}}{\partial x_1} - \frac{\partial \mathbf{K}}{\partial x_1}\boldsymbol{\alpha} = \begin{bmatrix} -\frac{\partial}{\partial x_1}\begin{bmatrix} K_{11}^{e,j} & \mathbf{0} \\ K_{21}^{e,1} & K_{22}^{e,1} \end{bmatrix} & \\ & \mathbf{0} \end{bmatrix} \begin{bmatrix} \alpha_{1:8} \\ \mathbf{0} \end{bmatrix}, \tag{17}$$

when $j \geq 2$,

$$\frac{\partial \mathbf{f}}{\partial x_j} - \frac{\partial \mathbf{K}}{\partial x_j}\boldsymbol{\alpha} = \begin{bmatrix} \mathbf{0} & & \\ & -\frac{\partial K^{e,j}}{\partial x_j} & \\ & & \mathbf{0} \end{bmatrix} \begin{bmatrix} \mathbf{0} \\ \alpha_{4j-3:4j+4} \\ \mathbf{0} \end{bmatrix}. \tag{18}$$

The $\partial K^{e,j}/\partial x_j$ value can be obtained by differentiating $K^{e,j}$ with respect to x_j in Eq. (14). Subsequently, multiplying $\mathbf{K}^{-1}$ by N vectors can be efficiently performed using the adjoint method,[35] where an adjoint equation is defined as

$$\mathbf{K}^{\mathsf{T}}\boldsymbol{\lambda} = \left(\frac{d\eta}{d\boldsymbol{\alpha}}\right)^{\mathsf{T}}, \tag{19}$$

where $\boldsymbol{\lambda} \in \mathbb{C}^{(4N+4)\times 1}$ is the adjoint vector. After obtaining $\boldsymbol{\lambda}$, the gradient is computed as

$$\frac{d\eta}{d\mathbf{x}} = \boldsymbol{\lambda}^{\mathsf{T}}\left(\frac{d\mathbf{f}}{d\mathbf{x}} - \frac{d\mathbf{K}}{d\mathbf{x}}\boldsymbol{\alpha}\right). \tag{20}$$

With the adjoint method, the cost of gradient computation becomes comparable with that of solving the spin trajectory.

C. Regularization

To ensure smooth pulse shapes, we apply the Helmholtz filter,[36] defined as

$$x^{s}(t) = R^{2}\frac{d^{2}x^{s}(t)}{dt^{2}} + x^{c}(t), \tag{21}$$

where R denotes the filter radius. The term $x^{c}(t)$ corresponds to the original control variables, while $x^{s}(t)$ denotes the filtered (smoothed) variables. By approximating the solution with linear shape functions, Eq. (21) is solved through a separate linear system,

$$\mathbf{K}_{h}\mathbf{x}^{s} = \mathbf{f}_{h}, \tag{22}$$

where the stiffness matrix elements are

$$K_{ij} = \int_{0}^{T} R^{2}\frac{d\phi_{j}}{dt}\frac{d\phi_{i}}{dt} + \phi_{j}\phi_{i}dt, \tag{23}$$

and the load vector elements are

$$f_{i} = \int_{0}^{T} x^{c}(t)\phi_{i}(t)dt. \tag{24}$$

The element stiffness matrix over the interval $[t_{j}, t_{j+1}]$ is

$$K^{e,j} = \begin{bmatrix} \int_{t_j}^{t_{j+1}} R^{2}\frac{d\phi_{j}}{dt}\frac{d\phi_{j}}{dt} + \phi_{j}\phi_{j}\ dt & \int_{t_j}^{t_{j+1}} R^{2}\frac{d\phi_{j+1}}{dt}\frac{d\phi_{j}}{dt} + \phi_{j+1}\phi_{j}\ dt \\ \int_{t_j}^{t_{j+1}} R^{2}\frac{d\phi_{j}}{dt}\frac{d\phi_{j+1}}{dt} + \phi_{j}\phi_{j+1}\ dt & \int_{t_j}^{t_{j+1}} R^{2}\frac{d\phi_{j+1}}{dt}\frac{d\phi_{j+1}}{dt} + \phi_{j+1}\phi_{j+1}\ dt \end{bmatrix}. \tag{25}$$

By substituting linear shape functions, the equation simplifies to

$$K^{e,j} = \begin{bmatrix} \frac{\Delta t}{3} + \frac{R^{2}}{\Delta t} & \frac{\Delta t}{6} - \frac{R^{2}}{\Delta t} \\ \frac{\Delta t}{6} - \frac{R^{2}}{\Delta t} & \frac{\Delta t}{3} + \frac{R^{2}}{\Delta t} \end{bmatrix}. \tag{26}$$

Since the control variables $\mathbf{x}^{c}$ are piecewise constant, the load vector is computed as

$$f_{i} = \begin{cases} \frac{\Delta t}{2}x_{1}^{c}, & i = 1, \\ \frac{\Delta t}{2}(x_{i-1}^{c} + x_{i}^{c}), & 2 \le i \le N, \\ \frac{\Delta t}{2}x_{N}^{c}, & i = N+1. \end{cases} \tag{27}$$

The Jacobian matrix that relates the smoothed variables to the control variables is

$$\frac{d\mathbf{x}^{s}}{d\mathbf{x}^{c}} = \mathbf{K}_{h}^{-1}\left(\frac{\partial \mathbf{f}_{h}}{\partial x_{1}^{c}}, \frac{\partial \mathbf{f}_{h}}{\partial x_{2}^{c}}, \dots, \frac{\partial \mathbf{f}_{h}}{\partial x_{N}^{c}}\right), \tag{28}$$

which yields

$$\frac{d\mathbf{x}^{s}}{d\mathbf{x}^{c}} = \frac{\Delta t}{2}\left[\mathbf{K}_{h}^{-1}\right]_{[1:N,1:N+1]}\begin{bmatrix} 1 & & & & \\ 1 & 1 & & & \\ & 1 & \ddots & & \\ & & \ddots & 1 & \\ & & & 1 & 1 \\ & & & & 1 \end{bmatrix}_{(N+1)\times N}. \tag{29}$$

For pulses expressed in Cartesian coordinates, an additional hyperbolic tangent scaling function is applied to constrain the waveform amplitude within $[-1, 1]$,

$$x(t) = \frac{1 - e^{-\kappa x^{s}(t)}}{1 + e^{-\kappa x^{s}(t)}}. \tag{30}$$

Here, κ controls the steepness of the transition period; a typical choice is $\kappa = 10$, which allows the pulse to reach its maximum amplitude. The gradient of the scaled waveform $\mathbf{x}$ with respect to the smoothed variables $\mathbf{x}^{s}$ is a diagonal matrix,

$$\frac{d\mathbf{x}}{d\mathbf{x}^{s}} = \mathrm{diag}\left(\frac{2\kappa e^{-\kappa x_{i}^{s}}}{(1 + e^{-\kappa x_{i}^{s}})^{2}}\right), \quad i = 1, 2, \dots, N. \tag{31}$$

By the chain rule, the gradient of the fidelity η with respect to the control variables $\mathbf{x}^{c}$ is given by

$$\frac{d\eta}{d\mathbf{x}^c} = \frac{d\eta}{d\mathbf{x}} \cdot \frac{d\mathbf{x}}{d\mathbf{x}^s} \cdot \frac{d\mathbf{x}^s}{d\mathbf{x}^c}. \tag{32}$$

III. NUMERICAL IMPLEMENTATION

The linear algebra was implemented in Liouville space using the irreducible spherical tensors as basis operators. The global stiffness matrix was assembled using the function `sparse`, where the index matrices and value matrix were generated separately, and a three-dimensional array was employed to vectorize the computation of the value matrix. The element-wise multiplications in Eq. (18) were vectorized using a diagonal block matrix. The details of matrix assembly and solving are provided in the supplementary material, Sec. S3.

The control variables are updated using MMA, a widely used approach for large-scale, constrained nonlinear optimization problems, such as topology optimization.[37,38] MMA is a gradient-based algorithm that leverages the values and gradients of the objective and constraint functions to iteratively construct and solve a sequence of convex subproblems. Each subproblem has a unique optimal solution that can be efficiently obtained via a dual approach.[39] To employ the MMA algorithm, the maximization of the ensemble fidelity is formulated as a least-squares problem, i.e., by minimizing the following expression:

$$f(\mathbf{x}^c) = \sum_{k=1}^{N_{\text{ens}}} (1 - \eta_k)^2. \tag{33}$$

ALGORITHM 2. Find an optimal control pulse shape.

```
Input: Parameters of the spin system; Pulse parameters
Output: Optimized control pulse $\mathbf{x}$
Initialize $\mathbf{x}^c \leftarrow$ rand($M, N$);  // Random initialization
Solve $\boldsymbol{\eta}_k$ from Eq. (15) and $d\boldsymbol{\eta}_k/d\mathbf{x}$ from Eq. (20);
for $iter \leftarrow 2$ to $iter_{max}$ do
    if $\overline{\boldsymbol{\eta}} \geq target$ then
        break;
    else
        Compute $f_k$ from Eq. (34) and $df_k/d\mathbf{x}^c$ from Eq. (32);
        Update $\mathbf{x}^c$ using MMA;        // Update control
         variables
        Solve $\mathbf{x}^s$ from Eq. (22) and $d\mathbf{x}^s/d\mathbf{x}^c$ from Eq. (29);
         // Smooth variables
        if $\mathbf{x}^c$ are Cartesian components then
            Solve $\mathbf{x}$ from Eq. (30) and $d\mathbf{x}/d\mathbf{x}^s$ from Eq. (31) ;
             // Scale variables
        else
            $\mathbf{x} \leftarrow \mathbf{x}^s$;
        Solve $\boldsymbol{\alpha}$ from Algorithm (1);          // Solve LvN
         equation
        Solve $\boldsymbol{\eta}_k$ from Eq. (15) and $d\boldsymbol{\eta}_k/d\mathbf{x}$ from Eq. (20);
         // Adjoint analysis
return $\boldsymbol{x}$;
```

In the implementation, the least-squares objective was reformulated by converting the infidelities into $2N_{\text{ens}}$ linear constraints while setting the objective function to zero,[40]

$$\begin{aligned} f_0(\mathbf{x}^c) &= 0, \\ f_k(\mathbf{x}^c) &= 1 - \eta_k, \quad k = 1, 2, \ldots, N_{\text{ens}}, \\ f_{N_{\text{ens}}+k}(\mathbf{x}^c) &= \eta_k - 1, \quad k = 1, 2, \ldots, N_{\text{ens}}. \end{aligned} \tag{34}$$

Algorithm 2 outlines the pseudocode for solving the optimal control problem in Eq. (4). The control variables $\mathbf{x}^c$ consist of M channels, each with N discrete values. Iteration proceeds until the average fidelity $\overline{\eta}$ reaches the target (e.g., 0.995) or the maximum number of iterations is reached. For an ensemble of spin systems, the mesh is kept identical across all members, so the index matrix of the stiffness matrix remains unchanged. Each ensemble member has an individual Liouvillian, and the corresponding stiffness matrix is assembled to evaluate the spin trajectory and its gradient. Handling an ensemble system can be efficiently accelerated using MATLAB's parallel computing capabilities. In contrast, processing the variables involves solving a separate linear system, executed only once per iteration. For phase optimization, the smoothed variables $\mathbf{x}^s$ define the pulse shape; for Cartesian components (x and y) optimization, $\mathbf{x}^s$ is further scaled to the range $[-1, 1]$.

IV. RESULTS AND DISCUSSION

A. Accuracy and speed

The accuracy and computational efficiency of the FEM approach for solving the single-spin system were evaluated. The step-by-step propagation method[2] is adopted as a standard reference, where the control gradient is computed using the AUXMAT. This referred method was executed using Spinach v2.8,[41] where step propagators are computed via the reordered Taylor expansion, summing low-order terms to machine precision (2.22×10^{-16} on a 64-bit machine). All computations were performed in MATLAB 2025b on a PC equipped with an AMD Ryzen Threadripper PRO 3955WX 16-Cores processor (base frequency: 3.90 GHz) and 256 GB of RAM. For benchmarking the speed of the FEM method, MATLAB's parallel pool was disabled to remove the influence of parallel computing.

The relative error of the spin trajectory is defined as

$$\epsilon_\rho = \frac{1}{N+1} \sum_{i=1}^{N+1} \frac{|\rho_i^{\text{F}} - \rho_i^{\text{P}}|}{|\rho_i^{\text{P}}|}, \tag{35}$$

where N denotes the number of time steps, and ρ_i^{P} and ρ_i^{F} are the ith spin vectors obtained from step-by-step propagation and FEM, respectively. Since the spin state vectors are normalized, $|\rho_i^{\text{P}}| = 1$. In addition, the relative error of the gradient is computed as

$$\epsilon_{\text{grad}} = \frac{1}{N} \sum_{i=1}^{N} \left| \frac{\nabla_i^{\text{F}} - \nabla_i^{\text{auxmat}}}{\nabla_i^{\text{auxmat}}} \right|, \tag{36}$$

where ∇_i^{auxmat} and ∇_i^{F} are the partial derivatives of the objective with respect to the ith control variable, computed via AUXMAT and FEM, respectively. The approximation error is mainly determined by the discrete step size $\|\mathbf{L}\|\Delta t$. In typical liquid-state NMR experiments, an RF amplitude of 10 kHz and a time step of 1 μs yield $\|\mathbf{L}\|\Delta t = 0.063$. In this analysis, $\|\mathbf{L}\|\Delta t$ was varied from 0.01 to 0.1, and for each value, 30 random pulse shapes were generated to compute the mean values of ϵ_ρ and ϵ_{grad}.

Figure 2(a) shows the benchmark results for linear and quadratic elements; using the linear elements, the spin-trajectory error increases from 10^{-6} to 10^{-2}, while the gradient error rises from 10^{-4} to 10^{-1}. Employing quadratic shape functions significantly reduces these ranges to 10^{-7}–10^{-4} for the trajectory and 10^{-6}–10^{-3} for the gradient. An average ensemble fidelity of 0.995 can be achieved with a trajectory error of less than 10^{-3}, which, for linear element approximations, requires $\|\mathbf{L}\|\Delta t \leq 0.06$. The difference between ϵ_ρ and ϵ_{grad} arises because in Eq. (35), $|\rho_i^{\text{P}}|$ is fixed at 1, whereas in Eq. (36), ∇_i^{auxmat} can become very small for some control variables and reaches the approximation error of the linear or quadratic elements, resulting in an amplified relative error.

The performance of the linear and quadratic elements was compared with the AUXMAT and second-order finite difference (FD) methods, where the propagators were approximated by truncating the Taylor series. The linear elements achieve accuracy comparable with the AUXMAT/FD results obtained using second-order truncation, while the quadratic elements show comparable accuracy with AUXMAT/FD using third-order truncation (see the supplementary material, Fig. S4). The corresponding wall-clock time as a function of time steps is presented in Fig. 2(b). When N ranges from 100 to 2000, the linear elements provide approximately a 7× speedup over FD-2nd, and the quadratic elements yield roughly a 3.5× speedup over the FD third-order approximation.

The same procedure was applied to Hermite elements using a piecewise-linear waveform, and the relative error of the Hermite approximation is shown in Fig. 2(c). Unlike the case of piecewise-constant waveforms, the accuracy of the Hermite discretization depends on the smoothness of the linear waveform. Increasing the Helmholtz filter radius R enforces smoother pulse shapes, reducing the error and exceeding the quadratic-element accuracy when $R = T/42$. In addition, cubic Hermite elements offer an accuracy intermediate to that of AUXMAT/FD methods using second- and third-order Taylor truncation (see supplementary material Fig. S5). The wall-clock time for evaluating gradients of the linear waveform is presented in Fig. 2(d), where the Hermite elements provide approximately a 10× speedup over FD second-order approximation when N ranges from 100 to 2000.

It is worth noting that the FEM wall-clock time is piecewise linear; this behavior arises because stiffness matrix assembly and linear solves are performed on large sparse matrices. As the number of time

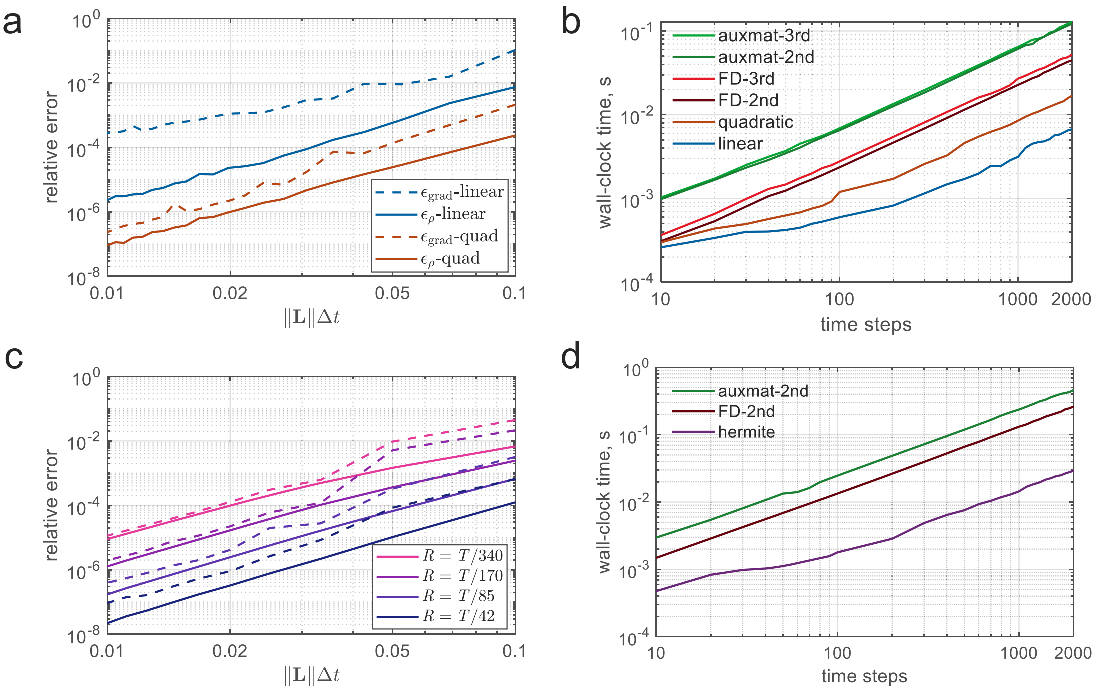

FIG. 2. Performance of FEM and the step-by-step propagation method for computing the spin trajectory and gradient in a single-spin system. **Piecewise-constant waveform**: (a) Relative error for the FEM linear and quadratic elements. (b) Wall-clock time for the FEM linear and quadratic elements, AUXMAT, and second-order finite difference (FD). The AUXMAT and FD methods used second- and third-order Taylor-truncated propagators, as indicated in the legend. **Piecewise-linear waveform**: (c) Relative error for the FEM cubic Hermite elements, where R denotes the Helmholtz-filter radius, which controls waveform smoothing. The solid and dashed lines denote spin-trajectory and gradient error, respectively. (d) Wall-clock time for the FEM Hermite elements, AUXMAT, and FD methods. The AUXMAT and FD methods employed second-order truncated propagators. Panels (a) and (c) use a pulse duration of $T = 0.5$ ms and a Liouvillian norm $\|\mathbf{L}\| = 2 \times 10^4$ rad s^{-1}, with N swept from 100 to 1000. Panels (b) and (d) fix $\|\mathbf{L}\|\Delta t = 0.063$ and sweep N from 10 to 2000.

steps increases, the working set eventually exceeds the CPU cache capacity. The computation thus transitions from a compute-bound regime, which is dominated by small dense matrix operations, to a memory-bound regime limited by RAM bandwidth. Consequently, a few jumps appear in the runtime curve, and its slope increases slightly in the large-N region.

B. State-to-state optimal control

The FEM combined with MMA was tested by optimizing a single-spin broadband excitation pulse, which transfers $\mathbf{I}_z$ to $\mathbf{I}_x$ over a 20 kHz offset range. The shaped pulse has a duration of 500 µs, discretized into 500 time bins, and a nominal amplitude of 10 kHz with ±20% variations. Gradients were computed using three methods: FEM with linear elements, the auxmat second order, and FD second-order approximations, which yield comparable numerical accuracy. Each method was repeated 20 times from different random initial guesses and their convergence rates are shown in Fig. 3(a). The similar convergence rates are primarily constrained by the MMA optimizer; its oscillatory convergence is analyzed in Sec. IV C. In terms of runtime, the linear elements achieved an order-of-magnitude speedup over auxmat second-order approximation, while the FD second-order approximation exhibits intermediate wall-clock time, as shown in Fig. 3(b).

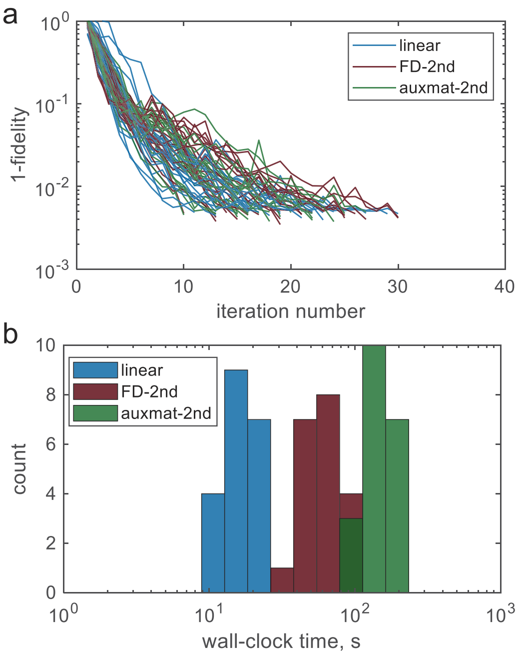

FIG. 3. Performance of the excitation pulse optimization for an ensemble single-spin system. (a) Convergence rate comparison for gradients computed using FEM with linear elements, AUXMAT, and second-order finite differences (FD). AUXMAT and FD used second-order Taylor-truncated propagators. Each method was repeated 20 times from different random initial guesses, and the MMA algorithm was used for optimization. (b) Histogram showing the time consumption of the three methods. The shaped pulse steers $\mathbf{I}_z$ to $\mathbf{I}_x$ with RF amplitude of 10 kHz and ±20% scaling ($n_{\mathrm{rf}} = 5$). A 20 kHz bandwidth was discretized into $n_{\mathrm{off}} = 51$ offsets, giving $N_{\mathrm{ens}} = 255$. The 500 µs pulse was piecewise constant with 500 segments, its amplitudes were fixed at 1, and its phases were optimized. The target ensemble fidelity was 0.995. To eliminate the influence of parallel computation, the parallel pool was disabled in MATLAB 2025b.

In the above-mentioned test, a single-spin system was constructed for each ensemble member, and all fidelities and gradients obtained from FEM, AUXMAT, or FD methods were provided to the MMA algorithm, in which the ensemble constraints were built by Eq. (34). When AUXMAT is combined with L-BFGS or Newton optimization, as implemented in Spinach, the Hamiltonians of the non-interacting subsystems can be assembled into a block-diagonal matrix, which allows the ensemble-averaged fidelity and gradient to be computed more efficiently. This block-diagonal acceleration was excluded from the comparisons.

C. Propagator optimization

The performance of MMA was tested against the L-BFGS and Newton–Raphson methods, with the latter two executed using Spinach v2.8. The test case involved optimizing a broadband universal rotation pulse, designed to realize the target propagator $\mathbf{U} = \exp\left(-\mathrm{i}\pi \mathbf{I}_x/2\right)$ across a 20 kHz offset range. The shaped pulse has a duration of 500 µs, discretized into 500 time bins, with a nominal amplitude of 10 kHz and ±10% scaling variations. The linear algebra was implemented in Hilbert space, where a unique target propagator favored by the optimization algorithm can be defined.[42] Unlike the step-by-step propagation in the GRAPE method, the FEM model approximates spin evolution directly using a linear combination of basis functions. As a result, the effective propagator is not explicitly constructed, rendering propagator optimization currently infeasible within the FEM framework. AUXMAT was used to compute the gradient for both MMA and L-BFGS as well as the Hessian matrix for the Newton–Raphson method; propagators were calculated using a Taylor series expansion truncated to machine precision. The convergence behavior shown in Fig. 4(a) indicates that L-BFGS achieves stable but slower convergence as the fidelity approaches the target. The Newton method converges more rapidly and stably, while MMA achieves a convergence rate comparable with that of the Newton–Raphson method, albeit with a non-monotonic curve. The wall-clock times, shown in Fig. 4(b), indicate that MMA completes the optimization faster than both L-BFGS and the Newton–Raphson methods.

The oscillatory behavior of the MMA algorithm arises from the implicit Hessian matrix of its first-order approximation. The empirical choices of the moving asymptotes implicitly generate an approximated, positive-definite diagonal Hessian (curvature), which may be inaccurate. For example, loose asymptotes yield smaller curvature and, consequently, an aggressive step that overshoots the local minimum. The algorithm then corrects this overshoot by moving back in the next iteration, leading to an oscillatory pattern. The modified variant, globally convergent MMA (GCMMA),[43] addresses this by introducing an additional inner iteration that plays a role analogous to a line search. This process forces more conservative approximations of both the objective and constraints, yielding slower but more stable convergence. However, each inner iteration requires recomputing the ensemble fidelities, whose cost is comparable with computing both fidelities and gradients together.

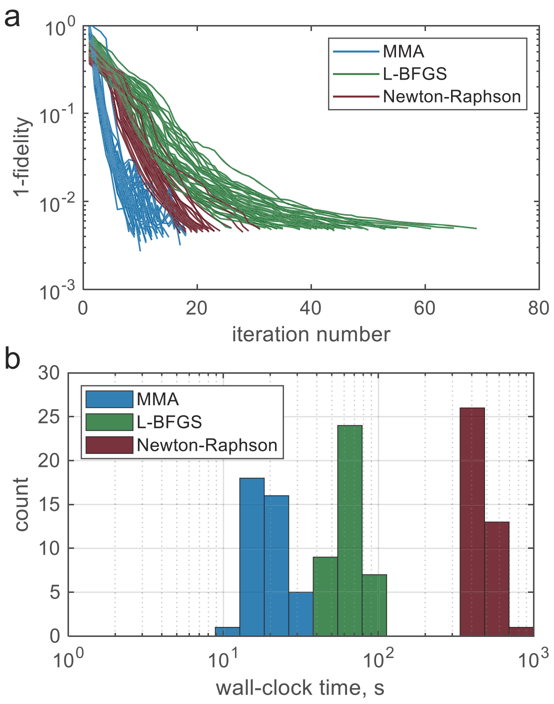

FIG. 4. Performance of implementing a universal 90°_x rotation for an ensemble single-spin system. (a) Comparison of convergence rates for the MMA, L-BFGS, and Newton–Raphson methods; each method was repeated 40 times using different random initial guesses, and AUXMAT was used to compute the gradient and Hessian. (b) Histogram of wall-clock time for three methods. The RF amplitude was 10 kHz with ±10% scaling ($n_{\text{rf}} = 5$). A 20 kHz bandwidth was sampled at $n_{\text{off}} = 51$ offsets, giving an ensemble size $N_{\text{ens}} = 255$. The 500 μs pulse used 500 piecewise-constant slices with unit-fixed amplitude, and the phases were optimized. Optimization targeted an ensemble fidelity of 0.995 and terminated at 100 maximum iterations. Ensemble gradient and Hessian evaluations were accelerated using 16 workers in MATLAB R2025b.

V. CONCLUSION

In this work, we employed the FEM method to solve the Liouville–von Neumann equation for a single-spin system. Achieving gradient accuracy comparable with the step-by-step propagation approach using second-order Taylor-truncated propagators, the use of linear elements provides an approximate order-of-magnitude speedup in gradient evaluation. In addition, the propagator optimization benchmark confirms that the MMA optimizer converges faster than L-BFGS, highlighting the potential of this approach for time-constrained optimal control problems.

With the adjoint method, gradient computation is as efficient as trajectory evaluation, which is similar to the case in step-by-step propagation. Hence, the computational cost is dominated by stiffness-matrix assembly and linear-system solving. While the 1-spin system attains the largest acceleration, this speedup reduces by ~4 for 2 spins (Fig. S7) and is expected to diminish further with increasing spin system size due to the runtime scaling with nearly the square of the nodal degrees of freedom in the current implementation. When the parallelization is used to accelerate the FEM and GRAPE, it is also worth studying their relative efficiency as a function of the number of degrees of freedom.

The oscillatory convergence behavior limits the applicability of MMA in high-fidelity scenarios, for example, 99.99%. A hybrid approach could use MMA to quickly reach an initial target and then switch to a more stable method for fine-tuning. Another direction is including spatial variables in the FEM model, either when diffusion becomes a degree of freedom[31] or when optimal control of fluid samples[44] is concerned.

SUPPLEMENTARY MATERIAL

The supplementary material includes the derivation of stiffness matrices for quadratic and Hermite elements and includes the matrix assembly and solution in MATLAB. It also provides performance benchmarks for the FEM, auxiliary matrix formalism, and second-order finite difference methods: specifically evaluating accuracy at small step sizes and computational speed for 1- and 2-spin systems.

ACKNOWLEDGMENTS

M.H. acknowledges support from the Joint Lab Virtual Materials Design (JLVMD) of the Helmholtz Association. J.G.K. acknowledges support from the ERC-SyG (HiSCORE, No. 951459). B.L. and J.G.K. acknowledge partial support from CRC 1527 HyPERiON. All authors acknowledge the Helmholtz Society's support through the Materials Systems Engineering program. The authors thank Dr. Neil MacKinnon for discussions and editing the manuscript.

AUTHOR DECLARATIONS

Conflict of Interest

J.G.K. is a shareholder of Voxalytic GmbH. The other authors have no conflicts to disclose.

Author Contributions

Mengjia He: Data curation (equal); Formal analysis (equal); Investigation (equal); Methodology (equal); Software (equal); Validation (equal); Visualization (equal); Writing – original draft (equal); Writing – review & editing (equal). **Yongbo Deng**: Conceptualization (supporting); Formal analysis (equal); Investigation (supporting); Methodology (equal); Software (equal); Supervision (supporting); Validation (supporting); Writing – review & editing (equal). **Burkhard Luy**: Conceptualization (supporting); Methodology (equal); Supervision (equal); Validation (supporting); Writing – review & editing (equal). **Jan G. Korvink**: Conceptualization (equal); Formal analysis (equal); Funding acquisition (equal); Investigation (equal); Methodology (equal); Project administration (equal); Resources (equal); Supervision (equal); Writing – review & editing (equal).

DATA AVAILABILITY

The data that support the findings of this study are available from the corresponding author upon reasonable request.

REFERENCES

[1] C. P. Koch, U. Boscain, T. Calarco, G. Dirr, S. Filipp, S. J. Glaser, R. Kosloff, S. Montangero, T. Schulte-Herbrüggen, D. Sugny, and F. K. Wilhelm, "Quantum optimal control in quantum technologies. Strategic report on current status, visions and goals for research in Europe," EPJ Quantum Technol. **9**(1), 19 (2022).

[2] N. Khaneja, T. Reiss, C. Kehlet, T. Schulte-Herbrüggen, and S. J. Glaser, "Optimal control of coupled spin dynamics: Design of NMR pulse sequences by gradient ascent algorithms," J. Magn. Reson. **172**(2), 296–305 (2005).

[3] I. Kuprov and C. T. Rodgers, "Derivatives of spin dynamics simulations," J. Chem. Phys. **131**(23), 234108 (2009).

[4] P. de Fouquieres, S. G. Schirmer, S. J. Glaser, and I. Kuprov, "Second order gradient ascent pulse engineering," J. Magn. Reson. **212**(2), 412–417 (2011).

[5] D. L. Goodwin and I. Kuprov, "Auxiliary matrix formalism for interaction representation transformations, optimal control, and spin relaxation theories," J. Chem. Phys. **143**(8), 084113 (2015).

[6] N. Leung, M. Abdelhafez, J. Koch, and D. Schuster, "Speedup for quantum optimal control from automatic differentiation based on graphics processing units," Phys. Rev. A **95**(4), 042318 (2017).

[7] M. Abdelhafez, D. I. Schuster, and J. Koch, "Gradient-based optimal control of open quantum systems using quantum trajectories and automatic differentiation," Phys. Rev. A **99**(5), 052327 (2019).

[8] S. Machnes, U. Sander, S. J. Glaser, P. de Fouquières, A. Gruslys, S. Schirmer, and T. Schulte-Herbrüggen, "Comparing, optimizing, and benchmarking quantum-control algorithms in a unifying programming framework," Phys. Rev. A **84**(2), 022305 (2011).

[9] J. H. M. Jensen, F. S. Møller, J. J. Sørensen, and J. F. Sherson, "Approximate dynamics leading to more optimal control: Efficient exact derivatives," Phys. Rev. A **103**(6), 062612 (2021).

[10] D. L. Goodwin and I. Kuprov, "Modified Newton-Raphson GRAPE methods for optimal control of spin systems," J. Chem. Phys. **144**(20), 204107 (2016).

[11] D. L. Goodwin and M. S. Vinding, "Accelerated Newton-Raphson GRAPE methods for optimal control," Phys. Rev. Res. **5**(1), L012042 (2023).

[12] Z.-J. Chen, H. Huang, L. Sun, Q.-X. Jie, J. Zhou, Z. Hua, Y. Xu, W. Wang, G.-C. Guo, C.-L. Zou, L. Sun, and X.-B. Zou, "Robust and optimal control of open quantum systems," Sci. Adv. **11**(9), eadr0875 (2025).

[13] K. Kobzar, T. E. Skinner, N. Khaneja, S. J. Glaser, and B. Luy, "Exploring the limits of broadband excitation and inversion pulses," J. Magn. Reson. **170**(2), 236–243 (2004).

[14] K. Kobzar, T. E. Skinner, N. Khaneja, S. J. Glaser, and B. Luy, "Exploring the limits of broadband excitation and inversion: II. Rf-power optimized pulses," J. Magn. Reson. **194**(1), 58–66 (2008).

[15] D. Joseph and C. Griesinger, "Optimal control pulses for the 1.2-GHz (28.2-T) NMR spectrometers," Sci. Adv. **9**(45), eadj1133 (2023).

[16] Z. Tošner, R. Sarkar, J. Becker-Baldus, C. Glaubitz, S. Wegner, F. Engelke, S. J. Glaser, and B. Reif, "Overcoming volume selectivity of dipolar recoupling in biological solid-state NMR spectroscopy," Angew. Chem., Int. Ed. **57**(44), 14514–14518 (2018).

[17] U. Rasulov, A. Acharya, M. Carravetta, G. Mathies, and I. Kuprov, "Simulation and design of shaped pulses beyond the piecewise-constant approximation," J. Magn. Reson. **353**, 107478 (2023).

[18] E. R. Lowe, S. Stoll, and J. P. Kestner, "Optimizing EPR pulses for broadband excitation and refocusing," J. Magn. Reson. **369**, 107807 (2024).

[19] U. Rasulov and I. Kuprov, "Instrumental distortions in quantum optimal control," J. Chem. Phys. **162**(16), 164107 (2025).

[20] D. L. Goodwin, P. Singh, and M. Foroozandeh, "Adaptive optimal control of entangled qubits," Sci. Adv. **8**(49), abq4244 (2022).

[21] S. Ehni and B. Luy, "BEBEtr and BUBI: J-compensated concurrent shaped pulses for 1H–13C experiments," J. Magn. Reson. **232**, 7–17 (2013).

[22] Z. Tosner, M. J. Brandl, J. Blahut, S. J. Glaser, and B. Reif, "Maximizing efficiency of dipolar recoupling in solid-state NMR using optimal control sequences," Sci. Adv. **7**(42), eabj5913 (2021).

[23] Y. Zhu, "Parallel excitation with an array of transmit coils," Magn. Reson. Med. **51**(4), 775–784 (2004).

[24] M. S. Vinding, B. Guérin, T. Vosegaard, and N. C. Nielsen, "Local SAR, global SAR, and power-constrained large-flip-angle pulses with optimal control and virtual observation points," Magn. Reson. Med. **77**(1), 374–384 (2017).

[25] M. S. Vinding, B. Skyum, R. Sangill, and T. E. Lund, "Ultrafast (milliseconds), multidimensional rf pulse design with deep learning," Magn. Reson. Med. **82**(2), 586–599 (2019).

[26] M. He, N. MacKinnon, D. Buyens, B. Luy, and J. G. Korvink, "Coherence locking in a parallel nuclear magnetic resonance probe defends against gradient field spillover," Magn. Reson. **6**(2), 173–181 (2025).

[27] M. He, D. Faderl, N. MacKinnon, Y.-T. Cheng, D. Buyens, M. Jouda, B. Luy, and J. G. Korvink, "A digital twin for parallel liquid-state nuclear magnetic resonance spectroscopy," Commun. Eng. **3**(1), 90 (2024).

[28] T. J. R. Hughes, *The Finite Element Method: Linear Static and Dynamic Finite Element Analysis* (Courier Corporation, 2012).

[29] G. Stang and G. Fix, *An Analysis of the Finite Element Method* (Prentice Hall, 1973).

[30] K. Svanberg, "The method of moving asymptotes—A new method for structural optimization," Int. J. Numer. Methods Eng. **24**(2), 359–373 (1987).

[31] G. P. Zientara and J. H. Freed, "The variational method and the stochastic–Liouville equation. I. A finite element solution to the CIDN(E)P problem," J. Chem. Phys. **70**(6), 2587–2598 (1979).

[32] P. Z. Gary and J. H. Freed, "The variational method and the stochastic–Liouville equation. III. Infinite elements for CIDN(E)P," J. Chem. Phys. **71**(2), 744–749 (1979).

[33] A. E. Stillman, G. P. Zientara, and J. H. Freed, "The variational method and the stochastic-Liouville equation. II. ESR spectral simulation via finite elements," J. Chem. Phys. **71**(1), 113–118 (1979).

[34] B. G. Galerkin, *Rods and Plates: Series in Some Questions of Elastic Equilibrium of Rods and Plates* (National Technical Information Service, Springfield, VA, 1968).

[35] Y. Cao, S. Li, L. Petzold, and R. Serban, "Adjoint sensitivity analysis for differential-algebraic equations: The adjoint DAE system and its numerical solution," SIAM J. Sci. Comput. **24**(3), 1076–1089 (2003).

[36] B. S. Lazarov and O. Sigmund, "Filters in topology optimization based on Helmholtz-type differential equations," Int. J. Numer. Methods Eng. **86**(6), 765–781 (2011).

[37] O. Sigmund, "Morphology-based black and white filters for topology optimization," Struct. Multidiscip. Optim. **33**(4-5), 401–424 (2007).

[38] J.-H. Zhu, W.-H. Zhang, and L. Xia, "Topology optimization in aircraft and aerospace structures design," Arch. Comput. Methods Eng. **23**(4), 595–622 (2016).

[39] K. Svanberg, "An algorithm for optimum structural design using duality," Math. Program. Study **20**, 161–177 (1982).

[40] K. Svanberg, *Some Modelling Aspects for the Matlab Implementation of MMA* (KTH Royal Institute of Technology, Stockholm, 2004).

[41] H. J. Hogben, M. Krzystyniak, G. T. P. Charnock, P. J. Hore, and I. Kuprov, "Spinach–A software library for simulation of spin dynamics in large spin systems," J. Magn. Reson. **208**(2), 179–194 (2011).

[42] K. Kobzar, S. Ehni, T. E. Skinner, S. J. Glaser, and B. Luy, "Exploring the limits of broadband 90° and 180° universal rotation pulses," J. Magn. Reson. **225**, 142–160 (2012).

[43] K. Svanberg, "A class of globally convergent optimization methods based on conservative convex separable approximations," SIAM J. Optim. **12**(2), 555–573 (2002).

[44] M. Alinaghian Jouzdani, M. Jouda, and J. G. Korvink, "Optimal control flow encoding for time-efficient magnetic resonance velocimetry," J. Magn. Reson. **352**, 107461 (2023).